https://ntrs.nasa.gov/search.jsp?R=20200001473 2020-03-28T19:20:08+00:00Z

Journal of Astronomical Telescopes, Instruments, and Systems

AstronomicalTelescopes.SPIEDigitalLibrary.org

Magnetic calorimeter option for the Lynx x-ray microcalorimeter

Thomas R. Stevenson
Manuel A. Balvin
Simon R. Bandler
Archana M. Devasia
Peter C. Nagler
Kevin Ryu
Stephen J. Smith
Wonsik Yoon

SPIE.

Thomas R. Stevenson, Manuel A. Balvin, Simon R. Bandler, Archana M. Devasia, Peter C. Nagler, Kevin Ryu, Stephen J. Smith, Wonsik Yoon, "Magnetic calorimeter option for the Lynx x-ray microcalorimeter," *J. Astron. Telesc. Instrum. Syst.* **5**(2), 021009 (2019), doi: 10.1117/1.JATIS.5.2.021009.

Magnetic calorimeter option for the Lynx x-ray microcalorimeter

Thomas R. Stevenson,[a,*] Manuel A. Balvin,[a] Simon R. Bandler,[b] Archana M. Devasia,[a,c] Peter C. Nagler,[a] Kevin Ryu,[d] Stephen J. Smith,[b,c] and Wonsik Yoon[a,e]
[a]NASA Goddard Space Flight Center, Detector Systems Branch, Greenbelt, Maryland, United States
[b]NASA Goddard Space Flight Center, High Energy Astrophysics Laboratory, Greenbelt, Maryland, United States
[c]University of Maryland, CRESST, Baltimore, Maryland, United States
[d]MIT Lincoln Laboratory, Lexington, Massachusetts, United States
[e]ASRC Federal Space and Defense, Beltsville, Maryland, United States

Abstract. One option for the detector technology to implement the Lynx x-ray microcalorimeter (LXM) focal plane arrays is the metallic magnetic calorimeter (MMC). Two-dimensional imaging arrays of MMCs measure the energy of x-ray photons by using a paramagnetic sensor to detect the temperature rise in a microfabricated x-ray absorber. While small arrays of MMCs have previously been demonstrated that have energy resolution better than the 3 eV requirement for LXM, we describe LXM prototype MMC arrays that have 55,800 x-ray pixels, thermally linked to 5688 sensors in "hydra" configurations, and that have sensor inductance increased to avoid signal loss from the stray inductance in the large-scale arrays when the detectors are read out with microwave superconducting quantum interference device multiplexers, and that use multilevel planarized superconducting wiring to provide low-inductance, low-crosstalk connections to each pixel. We describe the features of recently tested MMC prototype devices and simulations of expected performance in designs optimized for the three subarray types in LXM. © *The Authors. Published by SPIE under a Creative Commons Attribution 4.0 Unported License. Distribution or reproduction of this work in whole or in part requires full attribution of the original publication, including its DOI.* [DOI: 10.1117/1.JATIS.5.2.021009]

Keywords: microcalorimeter; detector; x-ray; array; paramagnetic; astrophysics.

Paper 18102SS received Nov. 1, 2018; accepted for publication Mar. 18, 2019; published online Apr. 9, 2019.

1 Introduction

One of the key instruments in the Lynx mission concept is the Lynx x-ray microcalorimeter (LXM).[1] Three detector features are essential to delivering Lynx science returns: large array formats (order 100,000 pixels) for large field-of-view, small pixel sizes of 50 and 25 μm for high angular resolution (1" and 0.5"), and energy resolution of 3 eV over the range of 0.2 to 7 keV and a resolution of 0.3 eV to cover the 0.2- to 0.75-keV band. Angular resolution to 0.5" will be essential to avoid source confusion, enabling, e.g., identification of growing supermassive black hole seeds in active galactic nuclei, and measurements of x-ray activity in young star forming clusters out to a much larger fraction of the Milky Way. Energy resolution of 0.3 eV, with 1" angular resolution, will, e.g., allow imaging and spectrally resolving the structure of hot galactic winds driven by supernovae and stellar feedback. The large field-of-view will enable deep extragalactic surveys to discover faint and rare sources. The candidate detector technologies being considered for LXM are transition edge sensors (TES) and metallic magnetic calorimeters (MMCs).

MMCs use a paramagnetic temperature sensor to measure the temperature rise, proportional to the x-ray energy, in a microfabricated x-ray absorber with a rapid thermalization time.[2] Dilute alloys of the rare earth element erbium in a gold matrix have especially suitable low-temperature properties for use as the MMC sensor material, and Au:Er MMCs have demonstrated excellent x-ray energy resolution, e.g., 1.56 eV full width half maximum (FWHM) at a x-ray energy of 6 keV.[3]

Because MMCs dissipate no bias power within the sensor, they have a natural advantage in terms of thermal design of large arrays operating at ultralow temperatures (≈30 mK). As array size is increased, one concern is a potential reduction in signal coupling due to increasing stray wiring inductance; however, superconducting interconnections with sufficiently low inductance and sensor coils with sufficiently high inductance can be made, using microstrip geometries and projection lithography, to enable arrays containing up to 8000 sensors and 100,000 x-ray absorbers, as required by LXM.[4] For multiplexing and readout, we assume use of "hydras" (multiple x-ray absorbers per temperature sensor)[5] and of microwave-multiplexed superconducting quantum interference device (SQUID) arrays[6] having good coupled energy sensitivity and an input inductance matched to the sensor plus stray inductance. We have recently completed fabrication[7,8] and initial tests[9] of LXM prototype MMC arrays using buried superconducting multilayer wiring,[10] fabricated underneath the MMC sensors and x-ray absorbers, to solve the wiring density problem at the scale for the LXM.

In this paper, we summarize the wiring and sensor designs for the three different subarrays in our large-scale LXM prototype MMC arrays with high inductance sensors and four-level buried wiring, performance measurements with initial small-scale arrays with two-level buried wiring, and simulations of expected performance of the large arrays for LXM.

2 MMC Sensor Designs for LXM

The LXM focal plane concept includes three subarray types, each with pixels optimized for different energy resolution,

*Address all correspondence to Thomas R. Stevenson, E-mail: Thomas.R.Stevenson@nasa.gov

angular resolution, and count rate capability according to mission science requirements.[1] MMC sensors can be designed for each subarray.

2.1 *LXM Subarray Types*

The "main array" will provide an energy resolution of better than 3 eV over the energy range of 0.2 to 7 keV, with pixel sizes that vary in scale from 0.5 arc sec in the innermost 1 arc min "enhanced array" to pixels that are 1.0 arc sec extending out to a 5 arc min field-of-view. A different subarray called the "ultra-high-resolution (UHR) array" will provide an energy resolution of 0.3 eV up to 0.75 keV in a 1 arc min region off to the side with 1 arc sec pixels.

The x-ray absorber pitches corresponding to 0.5 or 1.0 arc sec are 25 and 50 μm, respectively. The use of hydra designs with 5×5 absorbers per sensor is assumed for the main and enhanced arrays, and the UHR array has 1 absorber per sensor. The extent of the main and UHR arrays cover 60×60 sensors, whereas the enhanced array covers 24×24 sensors.

2.2 *High Inductance MMC Sensors*

With practical fabrication constraints on microstrip wiring linewidth, spacing, and insulation thickness, we estimated that the stray wiring inductance expected for a full-scale LXM main array would be ~2.5 nH for wiring within the array, plus 3.5 nH for fan-out to microwave SQUID multiplexer resonator arrays, or 6 nH totally. As described in Ref. 4, the expected stray inductance level motivated us to design and fabricate higher inductance MMC sensors, achieved by reducing the linewidth and pitch of the niobium sensor coils to 400 nm lines on an 800-nm pitch, for which the sensor inductance is 8 to 13 nH, depending on Nb thickness (200 to 500 nm). Our prototype variations include sensor designs with a range of meander pitches from 0.8 to 5 μm.

2.3 *Waffle Sensor Geometry for MMC Hydras*

A simple but fundamental rule for optimization of MMC sensitivity[2] is that the volume of the Au:Er sensor should be increased (for greater signal) until the (mostly magnetic) heat capacity of the sensor equals the heat capacity of the x-ray absorber (set by the operating temperature, absorber material, pixel area, and absorber thickness required to stop the maximum x-ray energy with high efficiency). To maintain good magnetic coupling with the reduced pitch in the high inductance sensor coils, the thickness of the Au:Er layer needs to be scaled proportionately to about 130 nm for 800-nm pitch. Given volume and thickness of the Au:Er, the requisite area of the sensor is determined and is found to cover most of the area of the main and enhanced hydra unit cells and a smaller fraction of the available area in the UHR sensors. Therefore, the heat capacity of the Au:Er layer need not be reduced below the optimal value when making the Au:Er thinner for good magnetic coupling to sensor meander coils with pitch as fine as 800 nm.

Consequently, we chose a waffle-shaped geometry for our MMC hydras in which a square hole in the Au:Er is introduced around the location of the support stem for each absorber, with sufficient size for the hole to contain a metallic (Au) thermal link between the absorber stem and the Au:Er temperature sensor, with a unique thermal conductance for the each link in the hydra so that differences in pulse shape allow one to determine the x-ray photon hit location. Figure 1 shows the Au:Er waffle shapes for the main and enhanced arrays. The UHR sensor has a simple annular shape with one hole in the Au:Er as shown.

The Au:Er material has a relatively low residual resistance ratio because it intentionally contains impurities (the erbium ions). As a result, the expected thermal diffusion time for a bare Au:Er waffle is not fast enough compared to the pulse rise times calculated for an initial hydra design. Figure 2 shows the improvement in thermal diffusion time when a pure Au layer is added on top of the Au:Er waffle to aid rapid thermalization. We included a 600-nm Au capping layer to speed up the time constant sufficiently for the hydra design without increasing the overall heat capacity significantly. In this calculation, we used the measured residual resistivity and specific heat of our sputtered Au:Er films, and the measured residual resistivity versus thickness for our electron-beam evaporated Au films, to compute the thermal diffusivity of the composite structure. Figure 2 shows the expected thermal diffusion time across a main array Au:Er waffle, estimated as distance across the waffle squared divided by diffusivity. A finite-element calculation of the 2-D thermal diffusion gave a similar conclusion that a 600-nm capping layer is suitable.

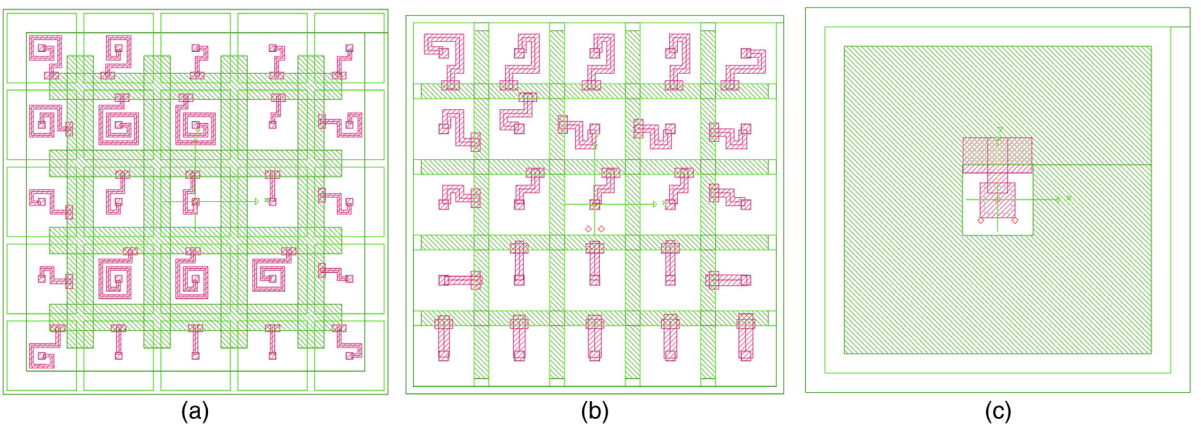

Fig. 1 Layout of (a) main, (b) enhanced, and (c) UHR MMC sensors. The Au:Er sensor (green shaded), Au thermal links (red shaded) between sensor and x-ray absorber support stems, and Au x-ray absorbers (green open) are shown. Absorber size is 50, 25, and 50 μm, respectively, for main, enhanced, and UHR sensors, whereas the overall hydra unit cells shown have sizes 250, 125, and 50 μm.

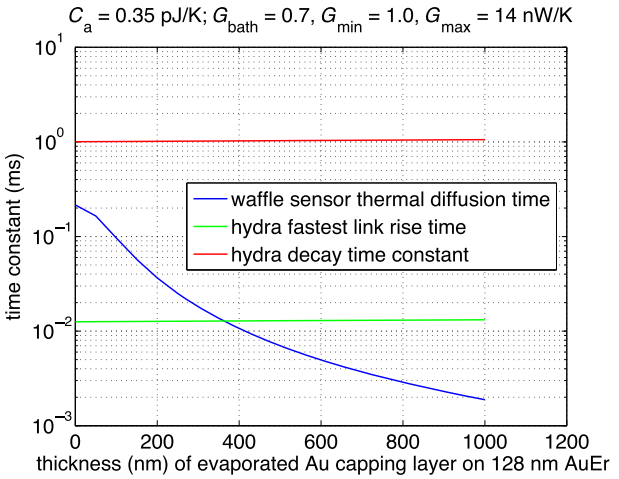

Fig. 2 Calculated thermal diffusion time across the Au:Er main array waffle sensor as a function of the thickness of a pure Au capping layer added to speed thermalization. The thermal diffusion time (curve) is compared with the fastest expected hydra pulse rise time (lower horizontal line) and the overall hydra decay time constant (upper horizontal line).

3 Microwave Readout

Microwave multiplexing approaches have the potential to read out around a thousand pixels per read-out amplifier. Microwave SQUID-based multiplexers (m-SQUIDs) have been developed at the University of Colorado (CU).[6] Demonstrations of read-out of gamma-ray and x-ray TES detectors using this technique show no energy resolution degradation from the nonmultiplexed case. We propose to use a similar scheme, but adapted to MMCs, where the requirements are different.

The circuit for reading MMCs with a microwave read-out is depicted in Fig. 3. Changes in the MMC temperature induce changes in the magnetization and, therefore, the inductance of the meander coil. This produces a change of current through the meander and also through the input coil to the rf-SQUID, thus changing the magnetic flux coupled to it. This in turn induces a change in the SQUID inductance and L_N and, consequently, also the frequency of the microwave SQUID resonator, determined by L_N, C_N, and R, which is typically in the range of 6 GHz. A single microwave feed-line can, in principle, read out a thousand pixels coupled to a thousand resonators uniformly spaced in frequency. The change in resonance frequency is sensed from changes in the microwave transmission and is amplified by a parametric amplifier[11] and a low noise high electron mobility transistor (HEMT) amplifier. The inputs to the rf-SQUIDs use filters to prevent microwave power escaping from the resonant circuit to the MMCs. Since the rf-SQUID is a nonlinear device that cannot effectively be operated in a flux-locked loop at these frequencies, a technique known as "flux-ramped modulation"[12] is used to provide a linear response. This technique uses a high frequency triangle wave to modulate the signal being input to the rf-SQUID over many Φ_0's at high frequency (higher than the MMC signal bandwidth 10 to 20 kHz). This provides a linear net response after demodulation in the room temperature electronics. The m-SQUID provides microwave bandwidth with power dissipation less than 10 pW/sensor.

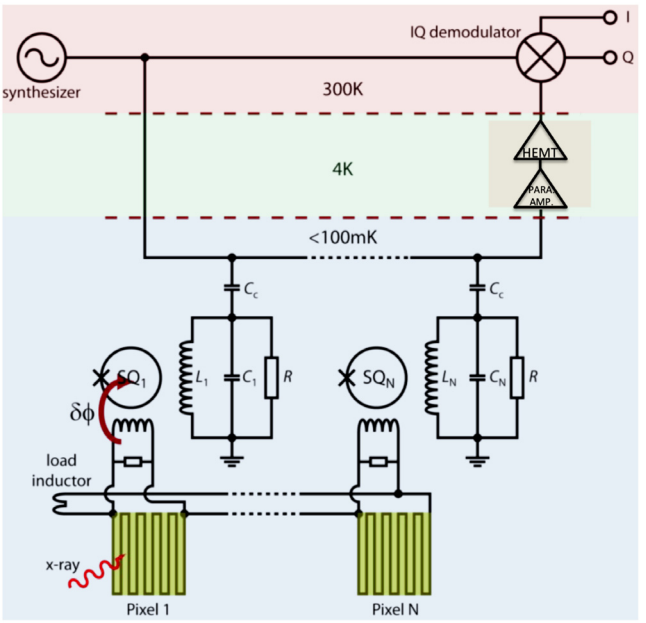

Fig. 3 Circuit for reading out an array of MMCs with a microwave readout.

The optimization of SQUIDs for MMCs differs from the optimization for TESs as they require the lowest possible flux noise in the SQUID. The figure-of-merit for SQUIDs that allows us to directly compare the performance of suitably matched rf and and dc-SQUIDs is the coupled SQUID energy sensitivity, which is usually expressed in units of the reduced Planck constant. The energy sensitivity is given by $\epsilon_s = \frac{L_i L_s}{M^2}\frac{S_\varphi}{2L_s}$, where L_s is the SQUID loop inductance, L_m is its input self-inductance, M is the input mutual inductance, and S_φ is the power spectral density of flux noise. For the dc-SQUIDs used to date, the best broadband energy sensitivity is 40 $\hbar$, although this increases at low frequencies. Achieving a similar level energy sensitivity for rf-SQUIDs should be possible, but so far SQUID resonators have not been designed with this in mind. With the low noise multiplexed read-out envisaged, the effective noise temperature of the HEMT amplifier needs to be very low and contributions to the noise of two-level systems (TLS)[13] also need to be very low. In preliminary rf-SQUIDs designed for TESs, both of these contributions are higher than is necessary.

At CU, a research goal for MMC readout is to design the microwave-SQUID to have energy sensitivity around 100 $\hbar$ by three key efforts. First, properly design them for MMCs, increasing the input inductance coupling to the SQUID resonators. Second, the HEMT amplifiers currently used need to be replaced with parametric amplifiers with much lower noise temperature than the 1.8 K for the HEMTs. Third, efforts can be made to minimize the TLS noise. By operating a flux-ramped modulation at a much higher frequency and across wider resonances than is currently used for TESs, the TLS noise will be substantially reduced. In addition, by taking advantage of resonator advances that have been taking place for MKIDs, it should be possible to reduce the TLS noise sufficiently to reach our sensitivity goal.

4 Multilayer Superconducting Wiring for LXM MMC Arrays

A planar, single-layer wiring approach would require many microstrip wires to pass between neighboring pixels, leading to technically challenging submicron wiring pitch values, especially given requirements on inductance, crosstalk, and critical

currents. Through-wafer via connections to a fan-out wafer located under the detectors has been demonstrated for some TES bolometer arrays,[14] but the need for smaller pixels and greater heatsinking in LXM make this approach impractical. Alternatively, in the approach described here, the use of buried layers of multilayer superconducting wiring is an attractive solution. This approach provides high density circuitry with feasible line widths, high fabrication yield even in large-scale circuits, excellent critical current density, the ability to reduce cross-talk with shielding ground planes, and a planarized top surface ideal for subsequent microcalorimeter fabrication.

4.1 *MIT Lincoln Lab Eight-Layer Multilayer Process*

A promising multilayer Nb process has been demonstrated by MIT/Lincoln Lab (LL). MIT/LL has developed a process that supports eight superconducting Nb metal layers for superconducting electronics.[15] Each Nb metal layer is defined by deep ultraviolet (DUV) lithography to achieve submicron line/space resolution. The submicron DUV photolithography requires high planarity of circuit layers because of the small depth-of-focus in modern photolithography. Therefore, the MLT/LL fabrication process utilizes chemical mechanical polishing to ensure all metal layers are deposited on a surface with topography height of less than 40 nm. The planarization also simplifies the addition of multiple metal layers by making the process modular—the process for the eighth metal layer can be the same as the process for the second metal layer. Through the use of this process, MIT/LL has integrated over 800,000 Josephson junctions in a single chip.[16] This high level of integration has been achieved for the first time in this technology and demonstrates the high-yield of high-density superconducting wiring at MIT/LL.

Multilayer buried wiring can also be utilized to lower the crosstalk without increasing the line-spacing of the wires. For high-density wiring with small linewidths, crosstalk can be an issue. By surrounding the signal lines with grounded shielding layer, crosstalk can be reduced by a large factor. The mutual inductance crosstalk between two superconducting Nb striplines, which are 1 μm apart and 0.25 μm wide, has been reduced to -41 dB using upper and lower ground planes, with data being in agreement with simulations.[17]

A third benefit of the multilayer buried wiring approach is that there is a planarized surface on top of the wiring on which to fabricate the main microcalorimeter pixels, with generally more space for the pixel designs and heat-sinking. This makes the subsequent fabrication process dramatically easier and even opens up pixel geometries. For example, MMC flux transformers and electrical crosstalk barriers could be introduced, which could not be realized on planar wiring.

4.2 *Automated (Algorithmic) Wiring and Sensor Layout*

In a first trial integrating buried wiring fabricated at MIT/LL with MMCs fabricated at Goddard Space Flight Center (GSFC), we took an existing mask layout, which we had developed for fabrication of small arrays (5×5) of high-inductance, nonhydra MMCs, and had the Nb microstrip and ground plane fabricated at MIT/LL using two Nb metal layers. In our second generation buried wiring prototype, connections to every sensor in the three LXM subarrays are implemented using four buried superconducting Nb layers. This provides high wiring density, low inductance, high yield, reduced cross-talk (shielding ground planes), and ability to fan out wires from enhanced and UHR arrays underneath main array pixels. However, to take advantage of the array scale enabled by the wiring process, we needed to approach the mask layout task differently.

Our LXM prototype has 55,800 x-ray pixels, thermally linked to 5688 sensors, with wires from each sensor brought outside the array perimeter. Since the complexity of the design exceeds the capability for manual mask layout, we automated the mask layout process with custom algorithmic techniques developed by one of us for a variety of detector fabrication projects at the Detector Systems Branch at Goddard.

The first step in the algorithmic approach was topological layout of wiring paths in muntins between pixels. The basic wiring scheme we employed has long been used in hand layout of small TES microcalorimeter arrays.[18] So that the required wiring pitch is relaxed, one can route the wires to attempt to equalize the number of wire-pairs in each muntin, with ideally at most $N/4$ wire-pairs in any muntin in an $N \times N$ sensor array. In determining wiring paths for one octant of a square array, starting from the muntin nearest the center line of the array, if routing wires from sensors near top of a muntin will exceed the $N/4$ goal, then one moves the path for those wires over to the next muntin to the right, and repeats this process for each muntin working from left (center line) to right (outer corner) in the octant. Success of the algorithm was shown for specific examples (e.g., for $N = 16$) worked out by hand but with no proof that the $N/4$ goal could always be achieved. For our LXM arrays with $N = 60$ or 24, this process is too tedious to complete manually but is rapidly solved with a computer algorithm. For even numbers N, we found that the $N/4$ goal is achieved only for $N \leq 18$. With the division we chose for upper and lower octants, we found that for $N = 20$ up to 38, one additional wire-pair per muntin is required to avoid wire paths being shifted outside the octant under consideration. For $N = 40$ up to 74, two additional pairs are required, whereas for $N = 76$ up to at least 200, three additional pairs suffice. Figure 4 shows the topological designs for $N = 60$ and 24. A data structure describing the topology can be saved and reused, e.g., for the main and UHR designs that both have $N = 60$.

Details of actual wire paths and sensor features were then also created algorithmically. In our main array design (Fig. 5), the Au:Er film is patterned in the "waffle" geometry described above, which leaves holes for a support stem to each absorber, and a customized Au thermal link between absorber and Au:Er. The high feature density of the LL process allows not only fabrication of sensor meander coils, with pitch as narrow as 0.8 μm, but also the packing of twin-microstrip wiring for the 60×60 sensor array into a single layer (over a ground plane) between hydras using 0.7 μm lines and 0.7 μm spaces (shown as 1.0 μm lines and 0.4 μm spaces in Fig. 5 but later modified).

The multilayer wiring provides even more benefits in our enhanced array design (Fig. 6). While the sensor meanders for this 24×24 array are on the same layer as for the main array, in order to have close proximity and therefore good magnetic coupling to the Au:Er, the wiring for the enhanced array uses two additional layers through near the center of an enhanced array hydra connect the meander to a deeper wiring layer hidden by an additional intervening ground plane. The advantages are: (1) fan-out of this array's wiring is beneath and hidden from the main array and (2) the intra-array wiring is also hidden from the sensor meander, allowing room for the desired sensor meander area, and for greater spacing between twin-microstrip pairs, thereby reducing crosstalk.

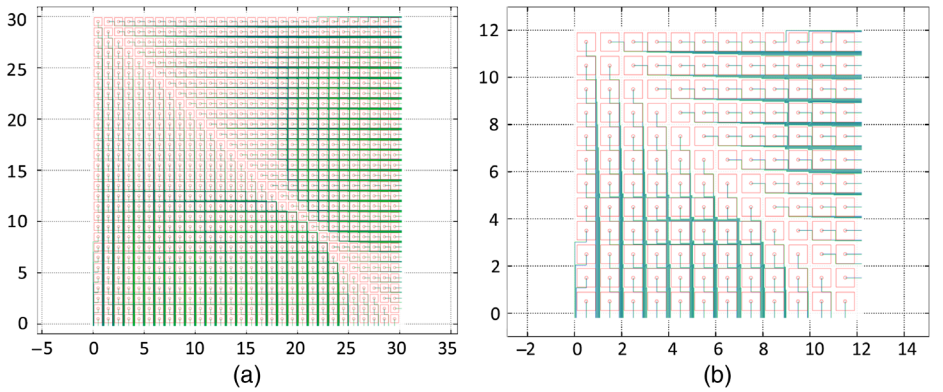

Fig. 4 Topological wiring schemes for one quadrant of an $N \times N$ sensor array for (a) $N = 60$ or (b) 24.

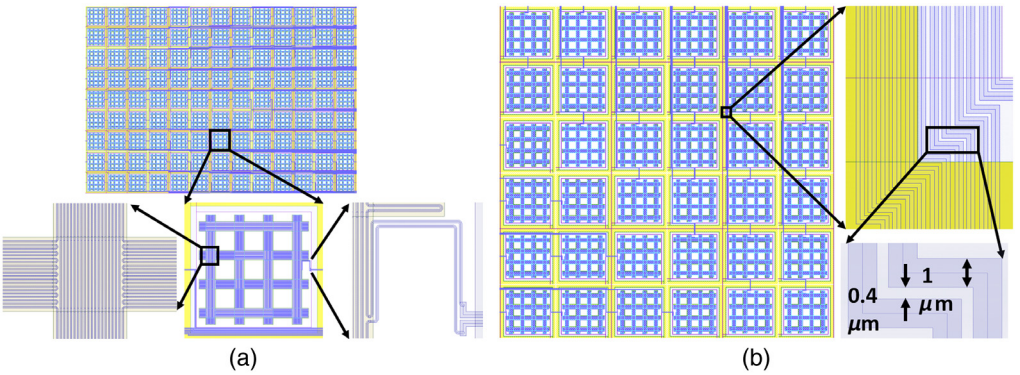

Fig. 5 (a) LXM main array sensor design with successive close-ups of one Au:Er waffle sensor, the Nb sensor coil that meanders to fill the area under the Au:Er waffle, and the interconnection to a twin-microstrip wire pair over a Nb groundplane in an adjacent muntin. (b) Details of the Nb wiring in the muntin, which is partially covered by a Au heat sinking grid.

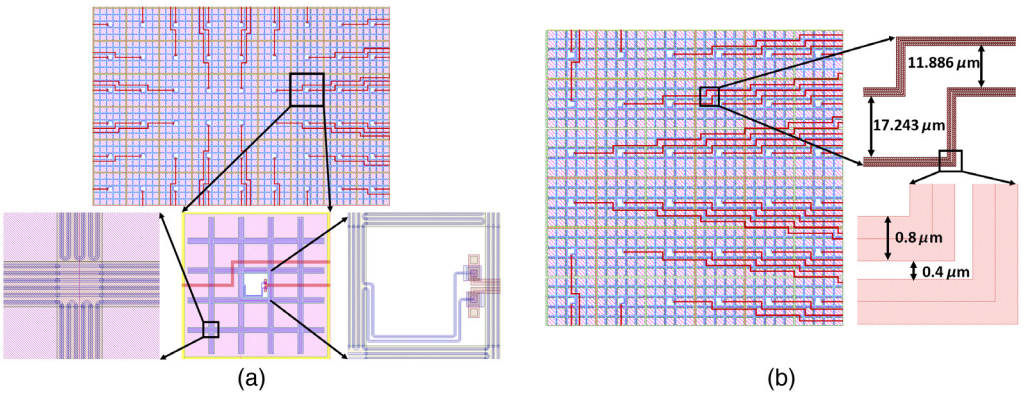

Fig. 6 (a) LXM enhanced array sensor design with successive close-ups of one Au:Er waffle sensor, the top level Nb sensor coil that meanders to fill the area under the Au:Er waffle, and the interconnection to lower wiring layers, through near the center of the waffle, to a twin-microstrip wire pair and ground plane. (b) Details of the Nb wiring in lower level muntins, which are shielded from the main array wiring and sensors by the intervening ground planes.

Our UHR design (Fig. 7) assumes the use of the same additional ground plane and wiring layers as the enhanced array. However, this 60×60 sensor array has sensor cell size 1/5 that of the main array, leading to an aggressive packing of the intra-array wiring, which could be relaxed if six Nb layers were used instead of four. For this first LXM prototype fabrication run, we chose to cover as much of the sensor cell area as possible with the Au:Er and meander coil so as to keep the sensor inductance >1 nH, even though this gives a sensor heat capacity higher than optimal. Even for the nonhydra UHR sensors, we included a thermal link, between the absorber and the Au:Er sensor, to enable us to control the size of the x-ray pulse slew rate, without introducing too much internal thermal noise [Fig. 1(c)].

The superconducting wiring from every sensor in the large arrays is brought out to the perimeter of the main array as it would be in LXM. Past that point, only selected sensors have

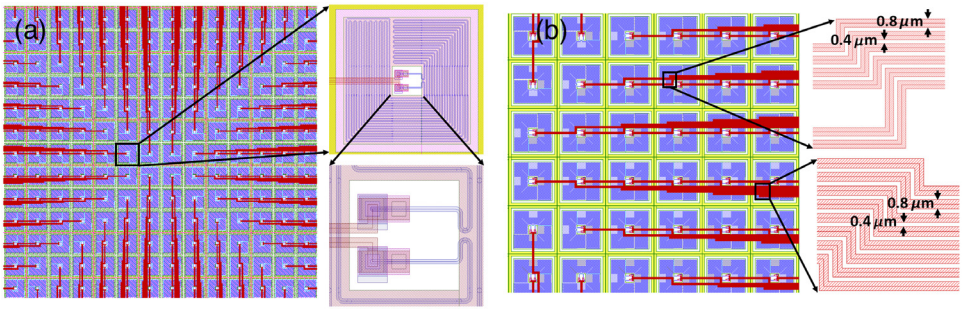

Fig. 7 (a) LXM UHR array sensor design with successive close-ups of one Au:Er annular sensor plus the top level Nb sensor coil that meanders to fill the area under the Au:Er annulus, and the interconnection to lower wiring layers, through vias near the center of the sensor, to a twin-microstrip wire pair and ground plane. (b) Details of the Nb wiring in lower level muntins, which are shielded from the main array wiring and sensors by the intervening ground planes.

their connections brought out to bond pads for SQUID readout to test this generation of devices. The fanout of the wiring is to two rows of 28 bond pad pairs along each long edge of the chip for a total number of 112 testable sensors. The spacing of the pads and the selection of testable pixels is arranged so that currently available NIST μMUX chips can connected with wire bonds to readout 20 sensors per cool-down, or alternatively PTB/Magnicon dc SQUID chips can be connected to readout eight sensors per cool-down, with a mixture of the three array types sampled in each case.

5 LXM MMC Arrays Prototype Fabrication

Fabrication of buried wiring is carried out on 200-mm diameter silicon wafers at MIT-LL. For our first, two-layer fabrication run, we kept the standard thickness of 200 nm for the SiO_2 insulation thickness for the final insulation layer that separates Nb meander coils from Au:Er. While nonoptimal for magnetic coupling, this was a conservative choice made to ensure high yield. In the second, four-layer run, the wafers in the batch were split between final oxide thickness values of 200, 50, and nominally 0 nm. After coring each 200-mm wafer to two 100-mm wafers and lapping to a standard wafer thickness, processing continued at the NASA GSFC Detector Development Laboratory to add the Au:Er sensor and its Au thermalization layer, a TiAu heat sink layer, and the electroplated Au mushroom x-ray absorbers. Further information about the fabrication process and resulting devices is given in Ref. 7. Here, we show a few illustrative images of the resulting devices.

As shown in Fig. 8, we fit two LXM array chips within each 22 mm × 22 mm projection lithography field on the wafers. One chip is 10 mm × 20 mm in size, whereas the other has two octants of the main array design deleted to give a 10 mm × 15 mm chip size. Figure 9 is a sequence of SEM images taken to show the evolution of the structures for main array hydras during processing.

6 Performance of MMCs with Buried Wiring

6.1 *Performance Characteristics of Initial Small Arrays with 2 Wiring Layers*

We have measured the performance of devices from our first buried wiring run, with high inductance sensors and two Nb layers. The prototype MMCs were fabricated with various geometries of 0.8-, 1.2-, 1.6-, and 5.0-μm pitch (line width is one half of the pitch). Each main array hydra has one 136 × 136 μm^2

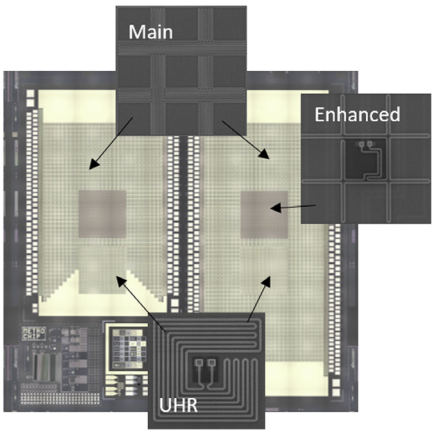

Fig. 8 Die layout of prototype MMC LXM array. The 22 mm × 22 mm reticle is divided into two chips differing only in size. Insets show locations of main array, enhanced array, and UHR array pixels.

Au:Er sensor and twenty-five 50 × 50 × 2.8 μm^3 gold absorber. As explained above, we separated the Nb coil and Au:Er sensor with a conservative 200 nm thickness of insulator. To expedite measurements, we also compromised by using the available PTB dc SQUIDs despite the inductance mismatch between their input inductance of 1.8 nH and our high-inductance meander coils. We measured this early version of buried wiring MMCs in a nonoptimal set-up currently purely for studying the different pitches and to verify the buried wiring process, and were pleased to see that the devices worked, and had a high critical current of 40 mA through the multilayer, fine-pitch wiring. We (i) measured Au:Er magnetization signal (change in SQUID flux from high temperature to the operating temperature) for various bias currents and sensor meander pitch, (ii) computed the total heat capacity C_{tot} and thermal conductance G_b of the MMC sensor to the heat bath from x-ray pulse heights and decay times, and (iii) measured energy x-ray resolution in a spectrum of Mn$K\alpha$ x-rays. The measured magnetization and heat capacity were in agreement with estimated values based on a numerical simulation of the Au:Er sensor at various temperatures. The measured thermal conductance of the pixels to the solid substrate, which consists of multiple layers of SiO_2 and Nb, was 50% of the value predicted from a simple acoustic mismatch model without accounting for the multilayer structure. Further details of the measurements and results are given in Ref. 9.

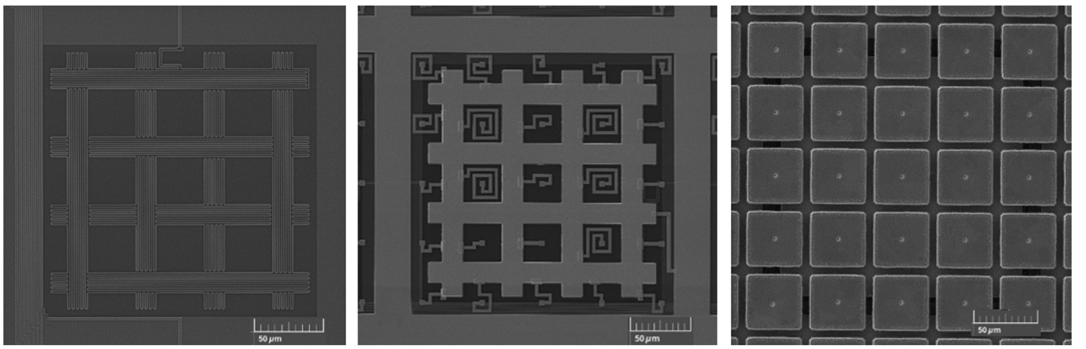

Fig. 9 Evolution of a main array hydra sensor during fabrication. (a) Sensor meander coil laid out in a waffle shaped pattern. (b) After deposition of Au:Er, heat sinking grid and hydra thermal links. (c) 5×5 hydra of 2.8-μm thick electroplated Au absorbers suspended over sensor. The overall hydra size is 250 μm $\times$ 250 μm.

6.2 *MMC Hydra Optimization and Projected Performance for LXM*

The first two wafers we have completed from the second generation, four-layer buried wire fabrication run used wafers with a 50 nm top insulation layer thickness, and are expected to give better energy resolution due to the improved magnetic coupling, and use of readout SQUIDs with appropriately matched input inductance. In addition, half the sensors in our large-scale arrays include Au thermal links to an intra-array heatsink to control the thermal conductance between sensor and heat bath and reduce thermal crosstalk. We have completed simulations of the expected response and energy resolution for the hydra sensors in the second-generation design, including the effects of position errors in the hydras. Figure 10 is an example of a magnetic field calculation from which the detector responsivity can be predicted.

Results of our hydra simulations show that the main and enhanced array sensor designs can achieve the Lynx 3-eV resolution goal, with good position resolution down to about 200 eV x-ray energies. Figures 11 and 12 show the results of simulations for the energy resolution and the accuracy of determining the x-ray absorption location in a 5×5 MMC main array for LXM, assuming a SQUID coupled energy sensitivity 100 $\hbar$ with input inductance matched to 0.8-μm pitch sensor with 50-nm insulation thickness, operating at 40 mK. The sensor meander coil inductance is 7.7 nH, whereas the stray inductance in the large array and fanout to the microwave SQUIDs is 5.9 nH. The SQUID input coil is assumed to have been designed to have self-inductance 13.6 nH for optimal matching to the sensor plus stray inductance. The erbium concentration is 900 ppm, and the meander current is 14.8 mA. The 25 conductance values of the thermal links in the hydra have been designed to minimize the worst-case probability of an error in determining the position

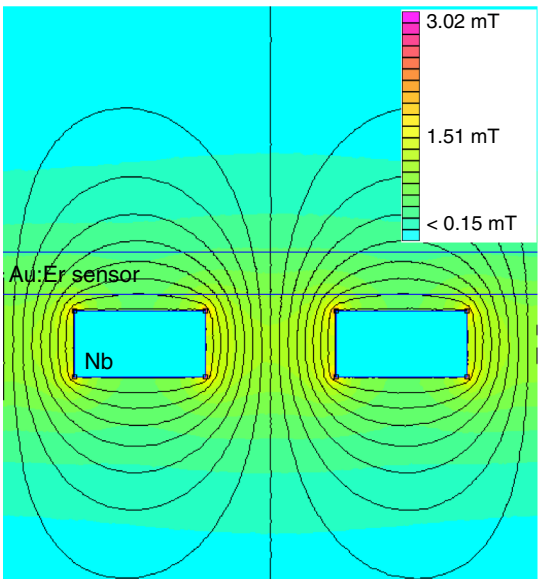

Fig. 10 Magnetic field lines in a cross-section through an MMC, calculated using a finite-element method approximating the Nb as perfect conductors, for 1 mA of current. Shown is the region around two Nb traces with counterflowing current in the middle of the coil. Nb traces are 400-nm wide and 200-nm thick. Coil pitch is 800 nm. Also shown is the region filled by a 130-nm thick Au:Er sensor 50 nm above the Nb, but the influence of the Au:Er on the magnetic field distribution is not included in the calculation.

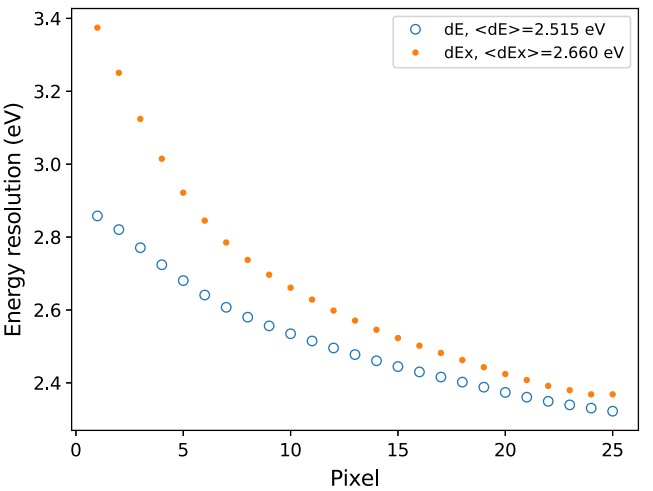

Fig. 11 Simulation predicting the FWHM energy resolution of the 5×5 hydra sensor with 800-nm pitch meander coils in the MMC main array in LXM. The energy resolution without errors in position correlation is dE, whereas dEx includes the effect of uncertainty in determining the x-ray absorption location in the 5×5 hydra for an x-ray energy of 200 eV. For x-ray energies much larger than 200 eV, the energy resolution approaches dE.

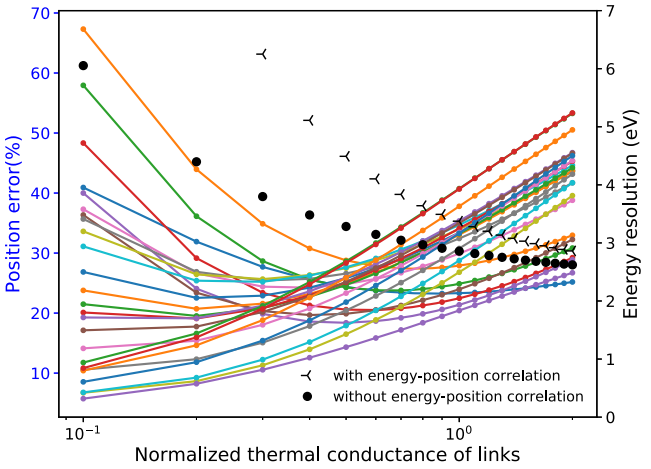

Fig. 12 Probability of an error in determining the position of the x-ray absorption in MMC hydra for the LXM main array, for 200 eV x-ray energy, as a function of the normalized link conductance. Also plotted is the worst energy resolution among the hydra pixels for high and low x-ray energies. The worst-case position error is minimized (29%) with an optimized value for the overall normalized conductance value 0.5 (and with an optimized distribution of the relative conductances for each of the 25 individual links). The energy resolution shown in Fig. 11 is for a normalized conductance value 1.0, for which the worst-case position error is 40%.

of the pixel hit by a 200 eV x-ray while not overly degrading the worst-case energy resolution among the 25 pixels. Here, the position error for a given pixel means the probability that a photon absorption event is incorrectly assigned a different pixel due to noise changing the best match to an optimal filter template.

To estimate the energy resolution and position error, we have used the correlated energy-position optimal filter algorithm.[19] From this algorithm, the theoretical energy resolution ΔE and the 1-sigma position resolution Δi are given as follows:

$$\Delta E = \frac{[\sum F_i' S_i']^{1/2}}{2[\sum F_i S_i \sum F_i' S_i' - (\sum F_i' S_i)^2]^{1/2}},$$

$$\Delta i = \frac{[\sum F_i S_i]^{1/2}}{2E[\sum F_i S_i \sum F_i' S_i' - (\sum F_i' S_i)^2]^{1/2}},$$

where S_i is the signal responsivity, S_i' is the derivative of S with respect to position i, F_i denotes the template optimal filter, and F_i' is the derivative of the filter with respect to position i. For the hydra, we have the same number of optimal filters as the number of pixels, and each optimal filter has a form, $F_i = S_i^*/N^2$, where N is noise component.

We calculated the position error and energy resolution for each pixel for hydra designs with various sets of thermal link conductances. Based on fabrication constraints, we bounded the ratio between highest and lowest link conductances, and then considered varying the overall conductance scale of a design characterized by the "normalized thermal conductance" parameter used in Fig. 12. (One can think of varying the normalized thermal conductance by changing the gold thickness used for the thermal links.) We iteratively distributed the relative conductances within the permitted range of ratios and varied the normalized thermal conductance so as to try to minimize the worst-case position error. As shown in Fig. 12, the position errors of all pixel are below 29% at a normalized conductance of 0.5. However, for that hydra design, the estimated energy resolution varies from 3.25 to 4.48 eV FWHM as the x-ray energy ranges down to 200 eV. As a practical trade-off between position error and energy resolution requirements, we chose the design for a normalized thermal conductance value 1.0, for which the energy resolution range is 2.85 to 3.37 eV FWHM and the maximum position error is 40% at 200 eV.

7 Conclusions and Outlook

Arrays of MMC x-ray microcalorimeters have been integrated with multilayer buried superconducting wiring to make arrays of the scale required by LXM. The MIT/LL process for fabrication of the wiring has the lithographic resolution to make both high inductance MMC sensor coils and dense microstrip wiring with high yield and excellent critical current densities. The ability to use multiple layers of wiring provides many advantages, and prototype arrays have been fabricated using just four metal layers out of the eight available in the MIT/LL process. Hydra sensors with 5×5 absorbers per sensor, a key ingredient in the LXM readout concept, have been designed and fabricated as part of the large-scale buried wiring demonstration. While the performance of the devices in the large-scale arrays has yet to be measured, data from the small-scale, two-layer wiring demonstration indicates the soundness of the buried wiring fabrication approach, and simulations provide the expectation that Lynx performance requirements can be met. In the course of developing the initial large-scale prototypes, a number of readily implemented refinements have already been identified that will be incorporated in successive generations, one example being the addition of a ground plane to "sandwich" the sensor between two Nb layers to increase magnetic coupling.[20,21] Over the next couple of years, using the techniques described here, we expect to dramatically increase the maturity and performance of large-scale cryogenic microcalorimeter arrays.

Acknowledgments

This work was supported with funding from the Internal Science Funding Model and the ROSES-APRA programs in the Astrophysics Division at NASA headquarters, and the Internal Research and Development Program at NASA/GSFC. MIT Lincoln Laboratory portion of the work is based upon work supported by the United States Air Force under Air Force Contract No. FA8702-15-D-0001. Any opinions, findings, conclusions or recommendations expressed in this material are those of the author(s) and do not necessarily reflect the views of the United States Air Force. Kevin Ryu acknowledges Eric Dauler, Jeffrey Mendenhall, and William Oliver for guidance, the Microelectronics Laboratory for the fabrication of the buried wiring wafers, and the Quantum Information and Integrated Nanosystems group for process monitoring and testing. The authors have no relevant financial interests in the manuscript and no other potential conflicts of interest to disclose.

References

1. S. R. Bandler et al., "The Lynx x-ray microcalorimeter—LXM," *J. Astron. Telesc. Instrum. Syst.* **5**(2) (submitted).
2. A. Fleischmann, C. Enss, and G. M. Seidel, "Metallic magnetic calorimeters," in *Cryogenic Particle Detection*, C. Enss, Ed., Topics in Applied Physics, Springer, Berlin, Heidelberg, Vol. **99**, pp. 151–216 (2005).
3. A. Fleischmann, "Metallic magnetic calorimeters," in *16th Int. Workshop Low Temp. Detect.*, Grenoble, France, Oral presentation (2015).

4. T. R. Stevenson et al., "Magnetic calorimeter arrays with high sensor inductance and dense wiring," *J. Low Temp. Phys.* **193**, 668–674 (2018).
5. J. P. Porst et al., "Development of position-sensitive magnetic calorimeter x-ray detectors," *AIP Conf. Proc.* **1185**, 599–602 (2009).
6. K. D. Irwin et al., "Microwave SQUID multiplexers for low-temperature detectors," *Nucl. Instrum. Methods Phys. Res. Sect. A* **559**, 802–804 (2006).
7. A. M. Devasia et al., "Fabrication of magnetic calorimeter arrays with buried wiring," *IEEE Trans. Appl. Supercond.* (2018).
8. T. Stevenson et al., "Design of magnetic calorimeter array with high density wiring," in *Appl. Supercond. Conf.*, Seattle, Washington (2018).
9. W. Yoon et al., "Design and performance of prototype magnetic calorimeter array for the Lynx x-ray microcalorimeter," *IEEE Trans. Appl. Supercond.* (2018).
10. S. K. Tolpygo et al., "Advanced fabrication processes for superconducting very large-scale integrated circuits," *IEEE Trans. Appl. Supercond.* **26**(3), 1100110 (2016).
11. C. Bockstiegel et al., "Development of a broadband NbTiN traveling wave parametric amplifier for MKID readout," *J. Low Temp. Phys.* **176**, 476–482 (2014).
12. J. A. B. Mates et al., "Demonstration of a multiplexer of dissipationless superconducting quantum interference devices," *Appl. Phys. Lett.* **92**, 023514 (2008).
13. J. Zmuidzinas, "Superconducting microresonators: physics and applications," *Annu. Rev. Condens. Matter Phys.* **3**, 169–214 (2012).
14. G. C. Hilton et al., "Fabrication of prototype imaging arrays for SCUBA-2," *Nucl. Instrum. Methods Phys. Res. Sect. A* **559**(2), 513–515 (2006).
15. S. Tolpygo et al., "Fabrication process and properties of fully-planarized deep-submicron Nb/Al/AlO_x/Nb Josephson junctions for VLSI circuits," *IEEE Trans. Appl. Supercond.* **25**(3), 1101312 (2015).
16. S. K. Tolpygo, "Superconductor digital electronics: scalability and energy efficiency issues," *J. Low Temp. Phys.* **42**(5), 361–379 (2016).
17. S. K. Tolpygo et al., "Developments toward a 250-nm, fully planarized fabrication process with ten superconducting layers and self-shunted Josephson junctions," in *16th Int. Supercond. Electron. Conf. (ISEC)*, Sorrento, Italy, pp. 1–3 (2017).
18. G. Hilton, "An ugly scheme for wiring the prototype 16 × 16 pixel array," NIST Memo (2005).
19. S. J. Smith, "Implementation of complex signal-processing algorithms for position-sensitive microcalorimeters," *Nucl. Instrum. Methods Phys. Res. Sect. A* **602**, 537–544 (2009).
20. A. Fleischmann et al., "Metallic magnetic calorimeters," *AIP Conf. Proc.* **1185**, 571–578 (2009).
21. C. Pies et al., "maXs: microcalorimeter arrays for high-resolution x-ray spectroscopy at GSI/FAIR," *J. Low Temp. Phys.* **167**(3–4), 269–279 (2012).

Thomas R. Stevenson is an electronics engineer at Goddard Space Flight Center. His doctoral research in physics at Stanford University improved the experimental upper limit on gravitational radiation flux and produced a novel microfabricated superconducting motion sensor. In postdoctoral research at the University of Maryland and Yale University, he collaborated on nearly quantum-limited dc SQUID amplifiers, electron phase coherence in mesoscopic systems, and RF single electron transistors. Currently, he develops detector technology for space flight applications.

Simon R. Bandler is a research astrophysicist at NASA's Goddard Space Flight Center. He received his BS degree in mathematical physics from the University of Sussex in the United Kingdom and his MS and PhD degrees in physics from Brown University in 1992 and 1996, respectively. He is the author of more than 100 journal papers. His current research interests include transition-edge sensor and magnetic x-ray microcalorimeters, x-ray astrophysics, and the ESA mission called Athena.

Kevin Ryu is a technical staff member in the Advanced Imager Technology Group at MIT Lincoln Laboratory. His expertise centers on device physics, fabrication, and modeling. He received his BE degree from the Cooper Union and SM and PhD degrees from MIT, authored numerous papers in the field of device physics, circuits, and process technologies for imagers. His current research interests are single-photon sensitive detectors such as low temperature detectors and avalanche photodiodes.

Stephen J. Smith received his MPhys degree in physics with Space Science and Technology and PhD in physics both from the University of Leicester, UK, in 2002 and 2006, respectively. He is an associate research scientist at University of Maryland Baltimore County (UMBC), working at NASA's Goddard Space Flight Center. He is an author of more than 100 published papers. His primary research interests are in the development of cryogenic detectors for x-ray astronomy applications.

Biographies of the other authors are not available.